Int J Coal Sci Technol (2018) 5(2):126–141
https://doi.org/10.1007/s40789-018-0194-5

# Numerical analysis of the failure process of soil–rock mixtures through computed tomography and PFC3D models

**Yang Ju[1,2] · Huafei Sun[3] · Mingxu Xing[3] · Xiaofei Wang[4] · Jiangtao Zheng[2]**

Received: 10 December 2017 / Revised: 28 December 2017 / Accepted: 1 January 2018 / Published online: 25 January 2018


**Abstract** Soil–rock mixture (SRM) is a unique type of geomaterial characterized by a heterogeneous composition and a complicated structure. It is intractable for the continuum-based soil and rock mechanics theories to accurately characterize and predict the SRM's mechanical properties. This study reports a novel numerical method incorporating microfocus computed tomography and PFC3D codes to probe the deformation and failure processes of SRM. The three-dimensional (3D) PFC models that represent the SRM's complex structures were built. By simulating the entire failure process in PFC3D, the SRM's strength, elastic modulus and crack growth were obtained. The influence of rock ratios on the SRM's strength, deformation and failure processes, as well as its internal mesoscale mechanism, were analyzed. By comparing simulation results with experimental data, it was verified that the 3D PFC models were in good agreement with SRM's real structure and the SRM's compression process, deformation and failure patterns; its intrinsic mesomechanism can be effectively analyzed based on such 3D PFC models.

**Keywords** Soil–rock mixture (SRM) · PFC3D model · Three-dimensional structure · Microfocus computed tomography (μCT) · Failure mechanism · Crack growth

## 1 Introduction

Soil–rock mixture (SRM) is a unique type of heterogeneous and discontinuous geomaterial that is composed of fine soil and coarse rock gravels. Structurally, SRM is a combination of a continuous microstructure between soil particles and a discontinuous macrostructure between soil particles and rock gravels, making the physical and mechanical properties of SRM distinct from those of soil and rock gravels (Zhong 1994; Yin 1998; Li et al. 2004; Liao et al. 2006). This unique geomaterial has captured attention in civil and infrastructure engineering applications, such as hydropower construction (Casagli et al. 2003), landslide monitoring (Li et al. 2007; Xu and Hu 2008), backfill engineering (Börgesson et al. 2003), and transportation engineering (Zhao et al. 2006), among other applications. Especially, geological hazards caused by landslide and debris flow occurred frequently and resulted in serious casualty and great economic losses (Heim 1882; Shang et al. 2001; Xu et al. 2009). Thus, it is important to well understand and accurately describe the strength, deformation and failure behavior of SRM to ensure the safety and stability of engineering applications.

To disclose the failure behavior and governing mechanisms of SRM, pioneer investigations have been conducted

✉ Yang Ju
juy@cumtb.edu.cn

[1] State Key Laboratory for Geomechanics and Deep Underground Engineering, China University of Mining and Technology, No. 1 University Avenue, Xuzhou 221116, China

[2] State Key Laboratory of Coal Resources and Safe Mining, China University of Mining and Technology, D11 Xueyuan Road, Beijing 100083, China

[3] School of Mechanics and Civil Engineering, China University of Mining and Technology, D11 Xueyuan Road, Beijing 100083, China

[4] State Intellectual Property Bureau of China, No. 6 Xitucheng Road, Beijing 100088, China

in both theory and engineering practice. Regarding in situ investigations, the deformation and failure properties of SRM were analyzed by the horizontal push-shear in situ tests, and the strength was reported to have a close relation with the rock shape and soil cohesiveness (He 2004). The concept of the average sliding surface, which is used to calculate the strength parameters, and the concept of the key diameter, which is important for determining the cohesion value, were put forward (Xu et al. 2006). The mechanical properties of SRM were found to be closely related to the rock content, mainly predominated by the staggered structure of the rock blocks (Xu et al. 2011). To probe the deformation and failure properties of SRM under cyclic loads, an in situ horizontal push-shear cycle test was performed (Xu et al. 2008a). The shear-strength calculating methods were proposed, and the liquefaction resistance and permeability properties of SRM were studied (Lin et al. 2004; Chen et al. 2012).

Studies involving laboratory tests were mainly focused on the impact of SRM components such as the composition and distribution of particle size, rock content and moisture condition on the macro-mechanical properties of SRM. For instance, a direct shear test was performed on rock–soil mixtures with different porosities, and the shear strength was found to depend largely on the aggregation degree of the rocks and soil (Vallejo and Mawby 2000). The rainfall-induced SRM landslide was reproduced by utilizing the self-developed laboratory experimental apparatus, and the observed failure phenomena revealed that the landslide failure mode depended greatly on the grain size and fine particle content (Wang and Sassa 2003). The effect of gravel content on SRM shear properties was also investigated (Kuenza et al. 2004; Xu et al. 2008b; Ouyang et al. 2010). Considering the nonlinear properties of SRM, the fractal theory was applied to study the strength properties of SRM (Shu et al. 2009). The needle penetration resistance, uniaxial compressive strength, tensile strength and elasticity modulus of clay-bearing rocks with different water contents were explored by laboratory tests, and a method for estimating the clay-bearing rock strength and deformability was proposed (Erguler and Ulusay 2009). The effect of saturation on the elastic wave velocity of clay–rock samples was studied, and the applicability of classical models was verified (Ghorbani et al. 2009). On the basis of high-resolution microfocus computed tomography (μCT) techniques, the generation, evolution and coalescence of internal fractures of SRM specimens with four different rock contents were explored, and the internal damage evolution mechanism and the influence of the rock content on SRM mechanical properties were analyzed (Sun et al. 2012, 2014a, b).

Different methods of numerical research, such as the finite element method (FEM), the finite difference method (DFM), and the discrete element method (DEM), were used to analyze the deformation and failure properties of SRM. For example, based on FEM, a mathematical model for the rain infiltration in the rock–soil slop has been established and solved (Liu et al. 2005). The large-scale direct shear tests of inhomogeneous SRM were simulated through FEM, and three types of failure models during the failure process were proposed (Xu et al. 2007). Based on DFM, the control function of the shape and distribution characteristics of a rock block on SRM deformation failure was explored by FLAC3D, and the relationship between elastic modulus and rock content was presented (You 2002). The thermo-hydromechanical behavior of Callovo–Oxfordian claystone was investigated by FLAC3D through a three-dimensional (3D) simulation of an in situ heating experiment, and a set of basic parameters involved in thermo-hydro-mechanical processes were discussed (Bian et al. 2012). Based on DEM, a stochastic PFC3D model of SRM was established, and a numerical experiment was conducted to verify the structural effect on the shear-push deformation damage (He et al. 2009). The failure process of SRM during a biaxial test was simulated using PFC3D (Cheng et al. 2010). A complete integration of the 3D fracture system, which linked the 3D fracture system into a 2D PFC model, was provided, and a 3D SRM model was subsequently formed to analyze the stress–structure interaction on the stability of vertical excavations in hard rock (Hadjigeorgiou et al. 2009). The relationship between moisture content and the process of loosening deposit forming in the mud-rock flow was revealed by PFC2D (Hu et al. 2010).

It is noteworthy that the geometry and distribution of rock gravels inside SRM are complex, and the most essential attribute is that SRM's composition and structure are highly heterogeneous and discontinuous, which causes not only the particularity of its deformation and failure mechanism but also the significant difference between analysis methods for SRM and those for conventional soil mechanics or rock mechanics. Conventional continuum-based theories of soil mechanics or rock mechanics are difficultly applied to accurately describe the deformation and failure behaviors of this special geomaterial whose properties are between those of homogeneous soil and those of rock fragments (Xu and Zhang 2013; Sun et al. 2014c). For those theories or analysis methods that were not based on the essential attribute of SRM, it would inevitably be difficult to provide scientific bases and effective ways to evaluate the stability of the geomaterial. Regarding SRM experimental research, restraints exist in both in situ field tests and laboratory tests. For instance, in situ field tests greatly rely on the experimental apparatus and environmental conditions, for which the test durations are limited. In most cases, field tests can only obtain the

macro mechanical properties, making it difficult to reveal the intrinsic meso-mechanism of the SRM deformation and failure process. Laboratory tests focusing on SRM's internal structures have been performed using laser scanning (Lanaro and Tolppanen 2002), digital photography (Yue et al. 2003) and CT techniques (Sun et al. 2012; Sun et al. 2014a). As a nondestructive technique, CT scanning is more preferable for studying SRM's complex structure. However, CT image processing is a challenging, time-consuming work, the quality of which has a large influence on the subsequent analytical results. In addition, it is expensive to obtain CT images of SRM's entire deformation and failure process through advanced 3D CT measurement techniques (Spanne et al. 1994; Coker et al. 1996).

Despite that numerical simulation has become a powerful tool to study SRM's deformation and failure properties, some challenges need to be tackled. Generally, most of SRM's numerical models cannot accurately represent the real, complex 3D structure of SRM. The problems of SRM's discontinuous structures and crack propagation also pose certain limitations to SRM numerical research (Sun et al. 2014b). Recently, PFC3D (Itasca_Consulting_Group 1999a, c) has been used to model complicated problems in solid mechanics and granular flow. Compared with other simulation programs, PFC is markedly superior for modeling rock size gradation and distribution, as well as the interaction of rock blocks inside SRM (Zhou et al. 2000; Fu et al. 2004; Luo et al. 2008; Fakhimi 2009; Ding et al. 2010, 2012). However, problems remain with respect to building PFC models that can represent SRM's real structure. At present, the most SRM models based on PFC are the stochastic structure models in which the rock blocks are generated according to the particles' self-organization on the macroscopic statistical level (You and Tang 2002; He 2004; Gan and Kamlah 2010; Liu et al. 2013). In some models, the rock blocks are created based on the two-dimensional (2D) representation of real SRM structure (Xu et al. 2007; Ding et al. 2010; Zhou et al. 2013). Few 3D PFC models with real rock geometry of SRM are available. However, in other research fields, PFC has also been utilized to simulate 3D blocks with irregular geometry. Lu et al. proposed a modeling method in which overlapping balls were used to form clumps using a simple procedure that controls the sphericity, angularity and surface texture of the clump to model the real ballast particles (Lu and McDowell 2007). Using a high-resolution scanner, You et al. (2008) captured the 2D microstructure of the asphalt concrete mixture, and a 3D model at a depth of 32 mm was generated by using four 2D models, each of which was duplicated 12 times, approximately 8 mm deep. To simulate the real asphalt mixtures of different aggregate gradations, shapes and angularity distributions, Yu and Shen established a DEM particle library with representative particles that were generated by clumping tens of balls together in PFC3D to match the scanning image obtained from the tests (Yu and Shen 2012, 2013). Subsequently, particles of different sizes could be selected from this particle library to generate the specimen model. Although great achievements have been made in modeling the real 3D materials containing blocks with irregular shapes, differences still exist between the internal structure of the generated model and the real sample, and it is difficult to determine the corresponding prototype tests of the real sample for comparison with simulations of these models. Therefore, generating PFC3D models that can reflect SRM's real heterogeneity and irregular structure, as well as conduct a numerical simulation of SRM's deformation, failure and crack propagation process based on such a real 3D model, remains a great challenge.

To solve the remaining problems in numerically characterizing the mechanical properties and failure mechanisms of SRM, we propose using a μCT technique to acquire the real structural information of SRM samples and constructing a 3D SRM model in PFC3D to represent SRM's real heterogeneity and irregular structure. By applying PFC3D code to simulate the entire failure processes of SRM cylinders under uniaxial compressive loads, we attained and analyzed the mechanical properties, including strength, elastic modulus, and deformability, and the failure behaviors, such as 3D crack initiation, growth and distribution, gravel movement, of SRM. The influences of rock ratios (0%, 10%, 20%, 30% and 50%) on the strength, deformation and failure modes, as well as its internal meso-mechanism, of SRM were discussed. In contrast to building a stochastic structural model, the proposed approach enables conducting numerical simulation and evaluation of SRM's properties based on real 3D structural models, which are undoubtedly closer to the actual situation.

This paper is organized as follows: Sect. 2 outlines the specimen preparation, CT scanning procedures and identification methods for acquiring structural information of SRM. Section 3 presents the SRM modeling method in PFC3D and the setup for numerical simulation of SRM's deformation and failure process under uniaxial compression tests. Section 4 discusses the simulation results from different aspects, including failure modes, crack growth and distribution, rock translation and rotation, and strength and modulus. To verify the simulation, the numerical results are compared with the CT experimental results. Conclusions are presented in Sect. 5.

## 2 Computed tomography identification and acquisition

### 2.1 Specimen preparation

Thirty cylindrical specimens of 33 mm in diameter and 66 mm in height were prepared. Fifteen of the specimens were tested to acquire the uniaxial compressive strengths, elastic modulus and deformation characteristics, ten were scanned to identify the internal fractures of SRM when loaded, and the remaining five were prepared as standbys. Five different rock ratios (i.e., 0%, 10%, 20%, 30%, and 50%) of SRM were tested. For every rock ratio, there were three specimens for uniaxial compressive tests and two specimens for CT tests. The rock ratio refers to the proportion of gravel mass to overall mass of SRM. Table 1 lists the ingredients of SRM. The soil component consists of 10% sand (0.5–1 mm) and 90% loess (< 0.5 mm). The rock component comprises small-size gravels (1–4 mm) and large-size gravels (4–7 mm). The water content refers to the ratio of water mass to soil mass, as shown in Table 1.

### 2.2 CT image processing and acquisition of structural information

To acquire the failure characteristics of SRM when loaded, we employed a CT machine to scan the entire structures of fractured specimens that experienced various loads. During the CT investigation, six loading stages of the uniaxial compression (i.e., unload, 40% pre-peak, 70% pre- peak, peak, 70% post-peak, and 40% post-peak) were applied simultaneously with CT scanning using a self-designed loading device, as shown in Fig. 1. At every loading stage, 1024 CT horizontal cross-section images of 550 × 550 pixels with a resolution of 72 μm per pixel were obtained. Figure 2, as an example, displays one original CT image of a 50% rock ratio specimen.

**Table 1** SRM ingredients

| | | | | | |
|---|---|---|---|---|---|
| Rock ratio (%) | 0 | 10 | 20 | 30 | 50 |
| Soil ratio (%) | 100 | 90 | 80 | 70 | 50 |
| Small-size rock ratio (%) | 0 | 7 | 14 | 21 | 35 |
| Large-size rock ratio (%) | 0 | 3 | 6 | 9 | 15 |
| Initial water content (%) | 15 | 15 | 15 | 15 | 15 |
| Final water content upon testing (%) | 6 | 6 | 6 | 6 | 6 |

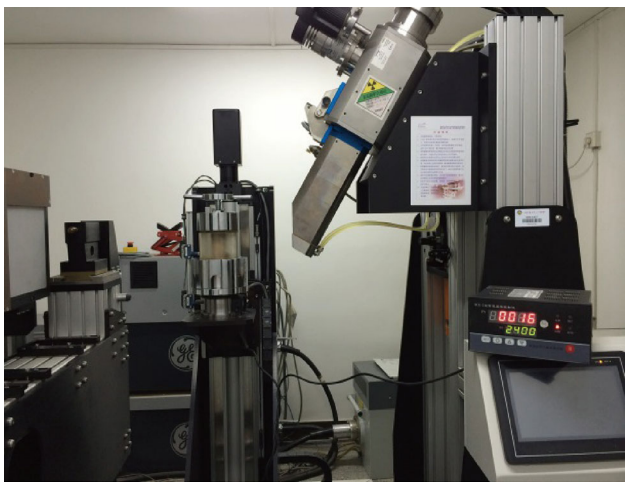

**Fig. 1** The loading apparatus mounted on the CT objective stage

The quality of the original CT images is far from being able to meet the requirements of precise image analysis and data acquisition. To improve image quality, we applied the special image processing measures as follows:

(1) Noise removal. There were several noises randomly distributed in the original CT images and some slight ring artifacts, which caused great difficulty in recognizing detailed SRM information. Therefore, a Gaussian filter was used to remove noises and ring artifacts first.

(2) Multiple-threshold segmentation. Every component of SRM, considered homogeneous, is supposed to have the same gray value. Through multiple-threshold segmentation, images were redrawn with three colors (black, gray and white). The black portions represent the fracture and outer space of the specimen; the gray portions indicate soil, and the white portions refer to rock gravels.

(3) Gray value compensation. Another problem was that the gray value in the CT image was found to be greater at the specimen edge. In other words, as the distance between a certain pixel point and the image center becomes larger, the gray value of that pixel tends to be large. This phenomenon was verified by the statistics obtained from the specimen at a rock ratio of 0%, whose gray values were supposed to be the same in the image but were not. To relieve this negative impact, based on the statistics, we calculated the pixel-value difference that each pixel requires to be compensated. A computer program was developed to automatically determine compensation for correcting gray-value of each point. The images were improved through the gray-value correction.

(4) Partial smoothing. A partial smoothing program was applied to smooth the rock edge without affecting detailed information on the fractures inside the SRM. This program was accomplished by applying the median filter to the image, which only includes the rock information that was extracted from the multiple-threshold segmented image. Then, the

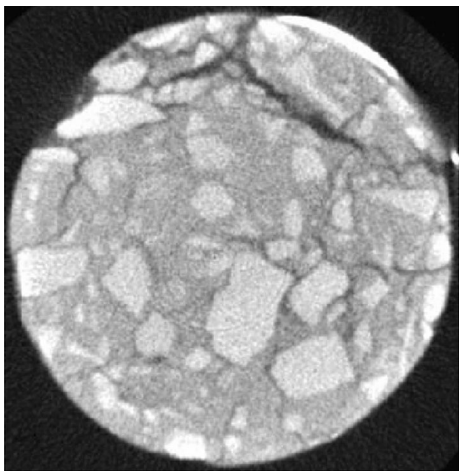

**Fig. 2** The original CT image

smoothed rock image and multiple-threshold segmented image were combined to obtain the result.

(5) Noisy-points elimination. Noisy points still existed in a disorderly fashion in the image after applied multi-threshold segmentation. To remove the noisy points, we applied the following measures to the preprocessed images. Define L as a length threshold. By detecting each portion with the same gray value in the image, the projected length ($L1$ and $L2$) in the $X$ and $Y$ directions of the portion were obtained. If both $L1$ and $L2$ were less than $L$, the color of that portion was replaced by its surrounding color.

(6) Background extraction. Using multi- threshold segmentation is not enough to separate all of the specimen components clearly. When the fracture and outer space of the specimen have almost the same performance when scanned by the CT technique, their gray values are close to each other, sometimes even mixed, which are difficult to distinguish from each other. Thus, a computer program of regional morphological segmentations was developed to identify and extract the fractures. As a result, the black portions represent the fractures, and the outer space was given the color of light gray.

Figure 3 illustrates the results of CT images processing and acquisition, including noise removal, multiple-threshold segmentation, gray value compensation, partial

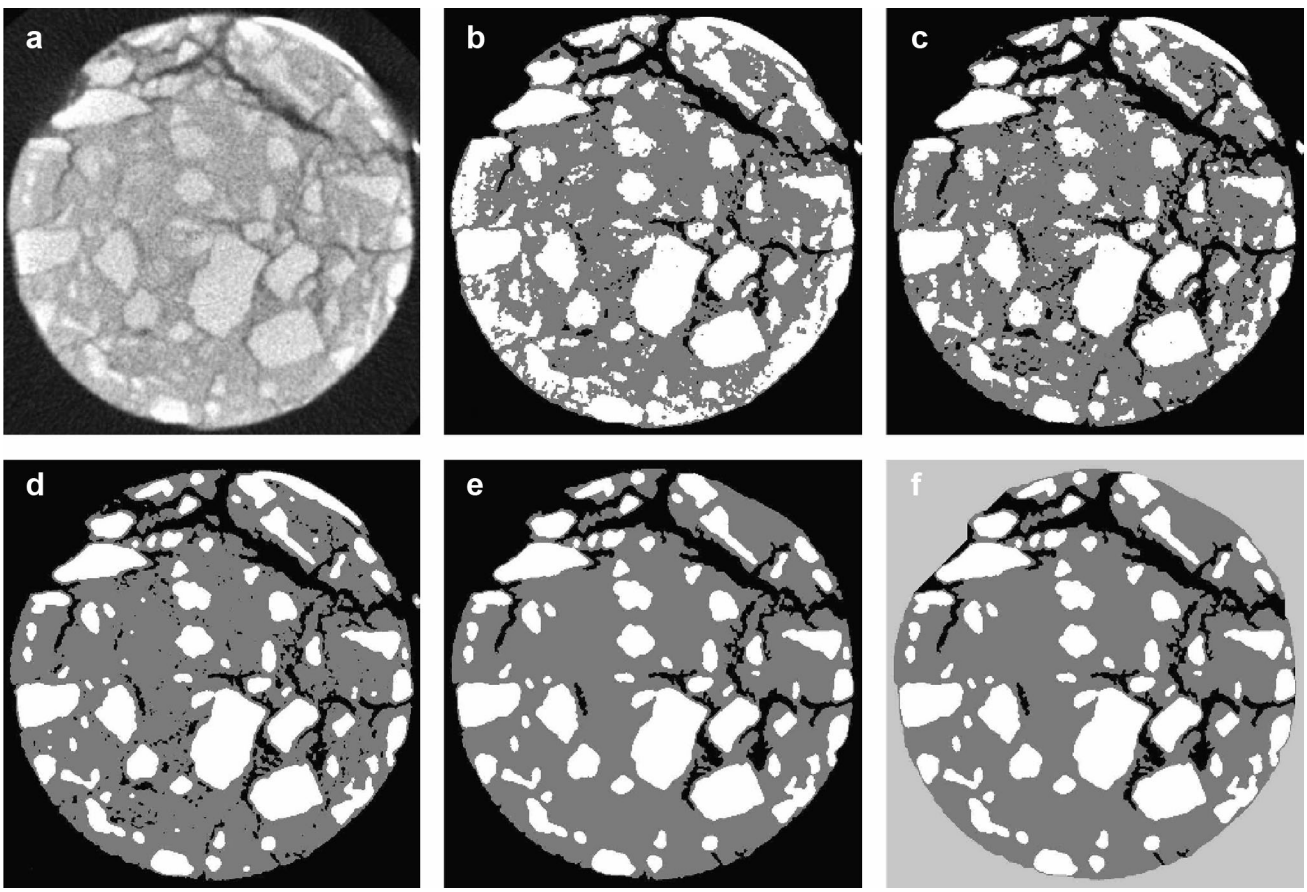


**Fig. 3** Illustration of CT image processing, identification and acquisition (**a**–**f** represent the imaging results of noise removal, multiple-threshold segmentation, gray value compensation, partial smoothing, noisy-particle elimination and background extraction, respectively)

smoothing, noisy- point elimination, and fracture extraction.

## 3 PFC3D modeling and simulation

### 3.1 PFC3D modeling

The SRM model can be considered the combination of a soil model and a rock model. The basic PFC3D modeling procedure is as follows: First, we build a soil model with balls randomly distributed; next, we select a certain group of balls that belong to the rock according to the real rock information; and finally, we combine this group of balls to represent the rock gravels. We will subsequently take one rock as an example to illustrate the specific modeling methods in PFC3D, as follows:

*Step 1*: Generate walls in PFC3D to build a closed cylindrical space, which has the same size as the actual specimen. Then, generate randomly distributed balls inside the space using the GENERATE command to create the pure soil model. The ball radius in our model is set at 0.5 mm; consequently, the soil model has 37,925 balls in total. This step is shown in Fig. 4.

*Step 2*: Input the processed CT images into the MIMICS platform to reconstruct the CT model, which has the same structure as the prototype specimen. Then, draw the volume mesh of a certain rock gravel to obtain the mesh nodes information, as shown in Fig. 5. By conducting the secondary development with FISH programming, the rock volume mesh is input into PFC3D.

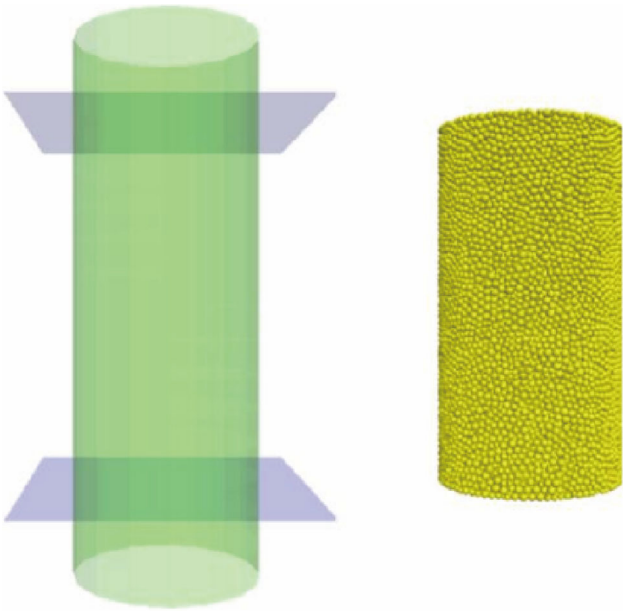

**Fig. 4** Soil particle model

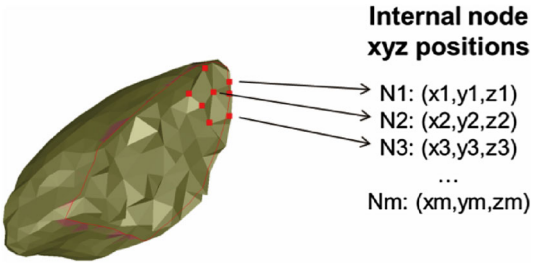


**Fig. 5** Volume mesh information of a rock gravel

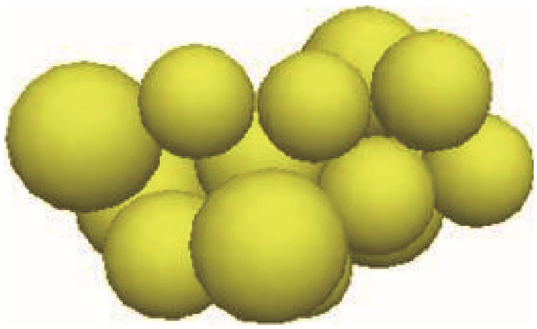

**Fig. 6** Single rock model

*Step 3*: Using FISH programming, the centroid information of every ball in the soil model is read, and the distance between the ball centroid and the rock mesh node is calculated. If this distance is sufficiently small so that the centroid is close enough to the node, this ball will be considered to belong to the rock. Using this method, a group of balls belonging to a certain rock will be selected.

*Step 4*: Use the CLUMP command to combine that group of balls to represent a certain rock gravel inside SRM, as shown in Fig. 6.

The above steps demonstrate how to build the single rock model. Using this method, we can draw the volume mesh of all the rock inside SRM together and then build the whole SRM model. Figure 7 shows the rock volume mesh of SRM with a 30% rock ratio, and Fig. 8 displays the final PFC3D model of SRM with a 30% rock ratio. In Fig. 8, the white color represents soil particles, and the other colors represent rock particles. In this SRM model, all the rock gravels are generated in one step, according to the CT reconstruction model. Each rock clump has its own unique shape resembling the counterpart rocks in the real SRM specimen. The biggest advantage is that simulation results conducted with this model can be compared with the experimental results produced by the corresponding specimen. Furthermore, the generating procedure is very simple because all the manipulating steps have been integrated into one program.

To verify the effectiveness of SRM PFC3D models, the cross section of the PFC3D model was cut out for

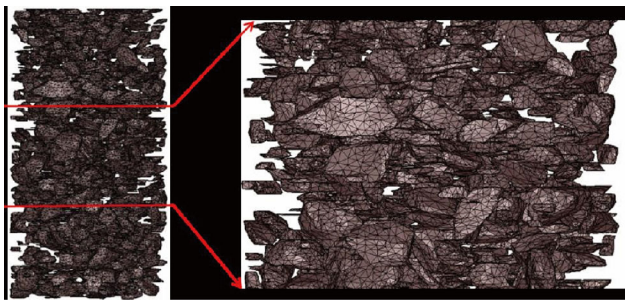

**Fig. 7** Volume meshes for rocks

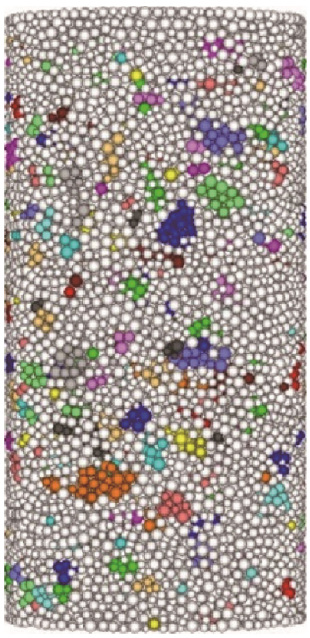

**Fig. 8** A complete PFC3D model of SRM with a 30% rock ratio. The white color represents soil particles, and the other colors represent rock particles

comparison with the CT image. Figure 9a illustrates one cross-section of the PFC3D model. Figure 9b displays the original CT image. In addition, Fig. 9c shows the comparison between the cross section of the PFC3D model and the prototype CT image. It is shown that the PFC3D model can reflect the real heterogeneity and irregular structure of SRM.

Some investigations indicate that SRM can be considered a system that comprises soil, rock and a soil/rock interface. The interface strength has a large influence on SRM's deformation and failure properties (Wang and Li 2014; Wang et al. 2014). Consequently, it would be reasonable to consider the soil/rock interface in the model. In PFC3D, there will be a "contact" between one ball and its neighboring ball. If two balls contact each other, the "contact" will be active. Otherwise, the "contact" will be inactive. By giving the "contact" a certain bond, the whole model will perform as an entirety. Alternatively, the balls in the model will perform discretely. Consequently, if a different contact type can be separated, the soil/rock interface will be modeled. Using FISH programming, the active "contacts" between soil particle and rock particle or between rock particle and rock particle were selected. Figure 10 demonstrates the 2D soil/rock interface and contacts, and Fig. 11 illustrates the 3D soil/rock interface in which panel (a) is the 3D rock geometry and panel (b) is the soil/rock interfaces and contacts surrounding the rock. By giving different bond strengths for the different contact types, the soil/rock interface will be modeled.

### 3.2 Calculation setup and parameters

The boundary condition was set according to the SRM uniaxial compressive tests. The lateral walls were deleted to eliminate lateral confinement. In addition, the bottom

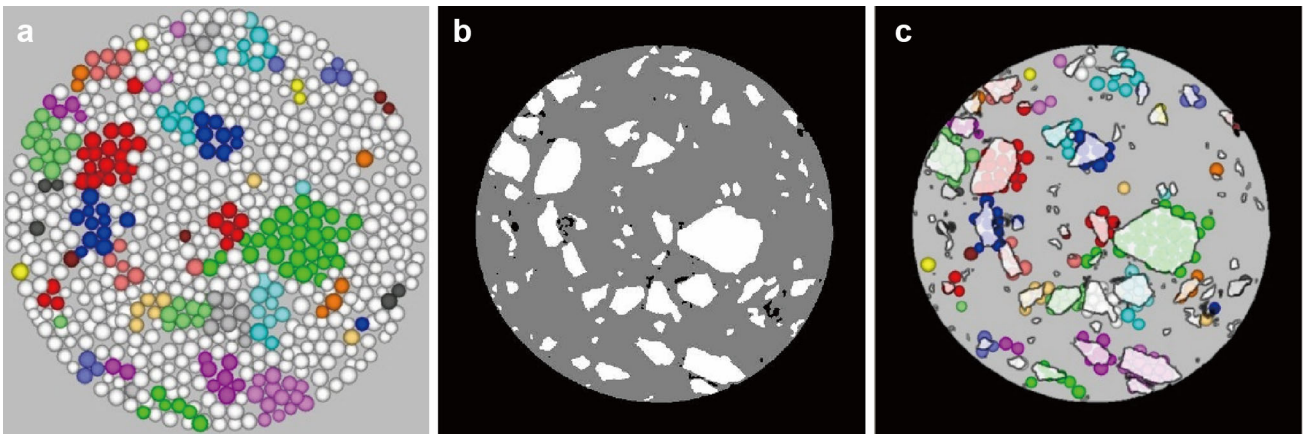


**Fig. 9** Comparison between the selected cross section of the PFC3D model and the prototype CT image, **a** the cross section truncated from the constructed PFC3D model, **b** the prototype CT image of the selected cross section, **c** comparing the rock gravels that are represented in PFC3D model with the real ones that are shown in the CT image

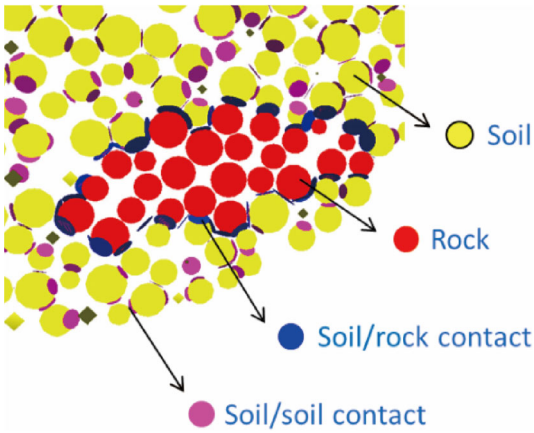


**Fig. 10** Illustration of 2D soil/rock interfaces and contacts

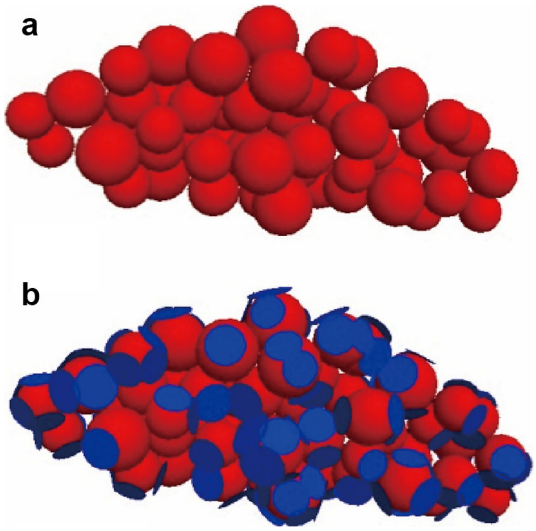


**Fig. 11** Illustration of 3D soil/rock interfaces and contacts, **a** 3D rock geometry, **b** soil/rock interfaces and contacts surrounding the rock

wall was fixed, while the top wall had a velocity to apply a displacement load.

In PFC3D, it is considerably difficult to determine the appropriate values of meso-level parameters of particles because the values cannot be directly obtained by laboratory tests, field measurements or theoretical calculations. Our solution is to numerically test the models by a trial and to adjust the values of the meso-level parameters of particles until the test results are in accord with those of real samples. In this study, the meso-level parameters of the SRM model in PFC3D were tested and obtained according to the method recommended by the Itasca Corporation Consulting Group and other scholars to save adjusting time (Itasca_Consulting_Group 1999b; Kulatilake et al. 2001; Potyondy and Cundall 2004; Cho et al. 2007; Guo et al. 2013). Considering that the stiffness of rock gravels in our test is much larger than that of soil, in the simulation, rock

**Table 2** Meso-level parameters of the soil model

| Particle parameters | | Contact bond parameters | |
|---|---|---|---|
| Particle density (kg/m$^3$) | 1776 | Mean normal strength (MPa) | 0.41 |
| Particle contact module (GPa) | 0.12 | SD of the normal strength (MPa) | 0.06 |
| Particle normal/shear stiffness | 3.5 | Mean shear strength (MPa) | 0.82 |
| Particle friction coefficient | 0.6 | SD of the shear strength (MPa) | 0.12 |

particles are combined by the CLUMP command making every rock model a rigid body that will not break apart. The "contact bond" mode is set to define the bond between two balls contacting each other. The meso-level parameters of the soil model applied in our simulation are shown in Table 2. In the natural state, different conditions may yield different interface types. Some interfaces have weak bonds with low strength, while others have strong bonds with high strength (Wang and Li 2014; Wang et al. 2014). In our simulation, it is difficult to determine the interface strength before specific investigation. Therefore, currently, we only set the parameters of the soil/rock contact bond to be the same as those of the soil/soil contact bond. Figure 12 illustrates the initial PFC3D models.

## 4 Simulation results and analyses

### 4.1 Failure processes and patterns

Figure 13 shows the failure patterns of SRM models with different rock ratios, in which blue and green disks represent tensile and shear fractures or cracks. The SRM models exhibit lateral expansion owing to the vertical displacement loading. The cracks tend to develop longitudinally and obliquely. Furthermore, in some models, shear zones form. Comparing the SRM failure patterns in PFC3D with those obtained through CT tests, as shown in Fig. 14, some similarities were observed in the failure patterns, thereby verifying the effectiveness of the simulation results.

### 4.2 Crack growth

In PFC3D, the bond between two particles will fail due to its normal or shear strength being exceeded. Then, the microcrack initiates, the geometry and location of which are determined by the sizes and current locations of the two parent particles from which the microcrack originated. This means that once two particles break, a microcrack initiates. However, due to the resolution limitation, CT scanning cannot reveal these tiny cracks. Therefore, to maintain

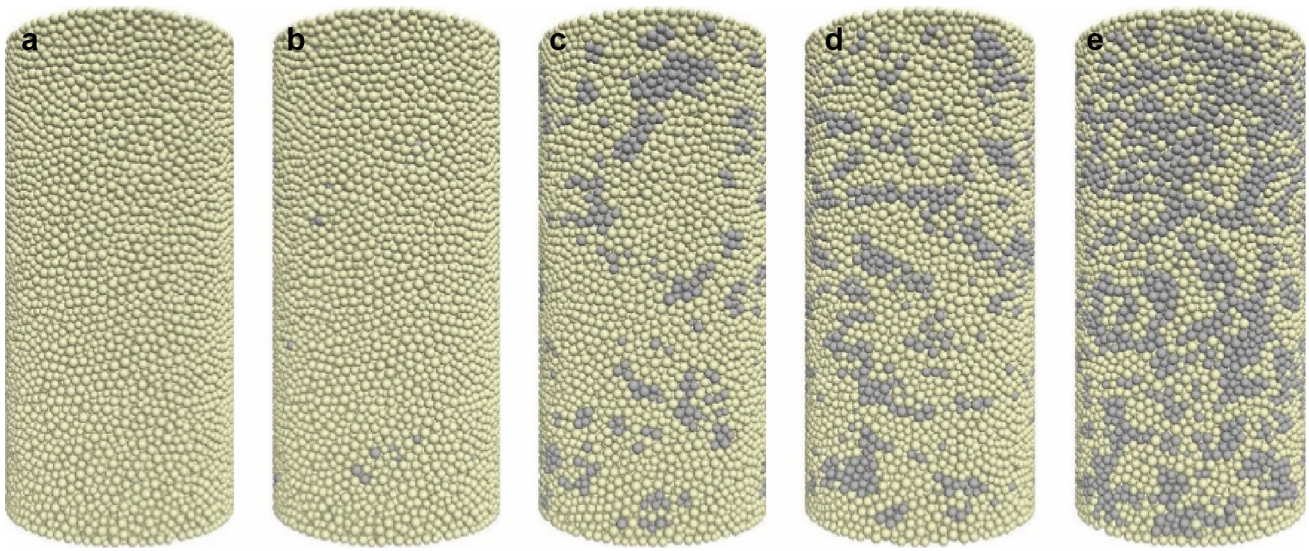


**Fig. 12** Initial PFC models (Light yellow and gray represent the soil particles and rock particles, respectively; **a–e** represent rock ratios of 0%, 10%, 20%, 30% and 50%, respectively)

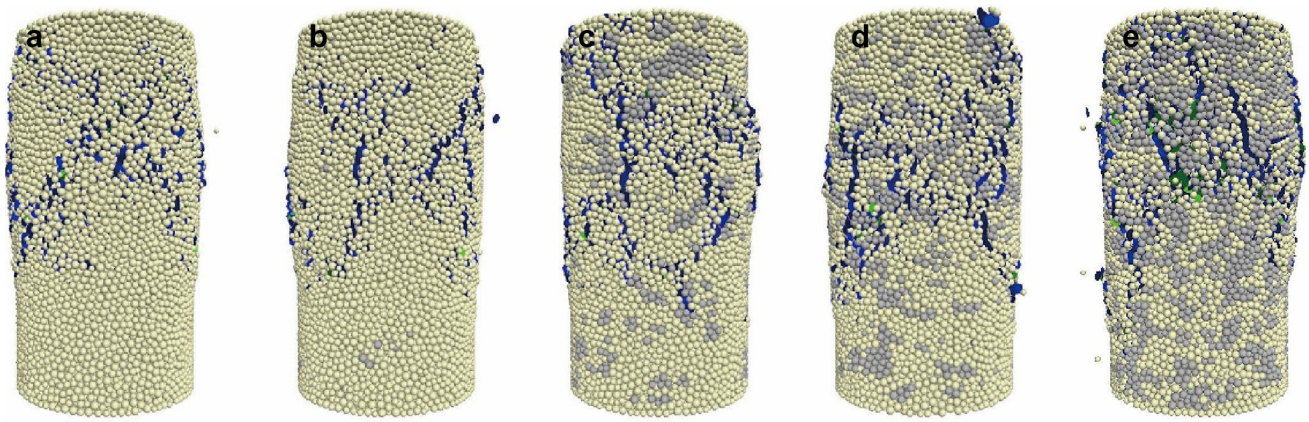


**Fig. 13** Failure patterns of the PFC3D models with various rock ratios (images **a–e** represent rock ratios of 0%, 10%, 20%, 30% and 50%, respectively)

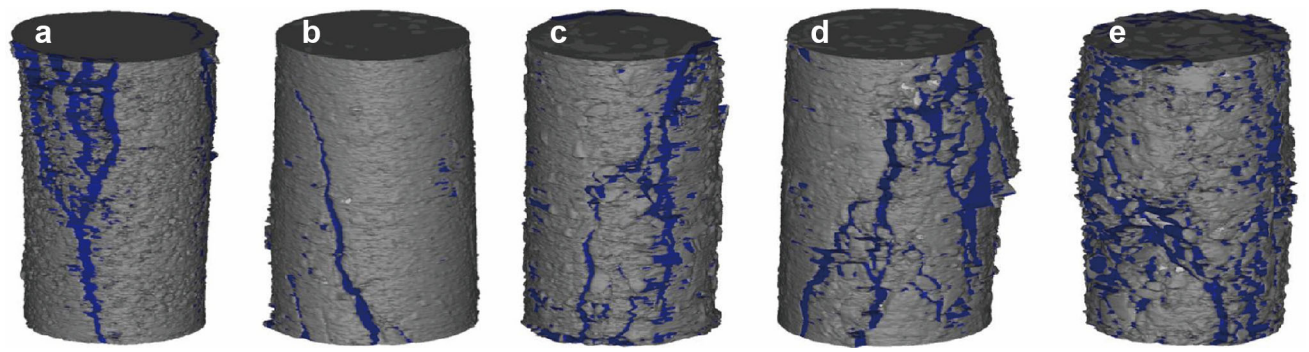


**Fig. 14** Failure patterns of the prototype models acquired through CT scan (images a–e represent rock ratios of 0%, 10%, 20%, 30% and 50%, respectively), in which dark blue color indicates the fractures or cracks when loaded

consistency with our CT tests, tiny cracks in PFC3D were eliminated by FISH programming. This means that if the distance between two broken particles in the PFC model is smaller than 72 μm (the resolution of our CT scanning), the microcrack will not appear in the simulation results.

To investigate the properties of crack growth, six loading stages were simulated, which are 40% pre-peak, 70% pre-peak, peak, 70% post-peak, 40% post-peak, and 20% post-peak, as shown in Fig. 15. According to the simulation results, there were few cracks before the peak load was reached; thus, we only selected certain simulation stages to show. Figures 16 and 17 illustrate the 3D crack growth in the PFC3D and CT scan tests, respectively. Moreover, similarities were found between these two groups of images. To further study the behavior of crack growth, a group of vertical sections of SRM models were attained, as illustrated in Fig. 18. By comparing cracks in different loading stages, it was found that before the peak load was reached, there were few cracks; however, once the peak load was reached, a few cracks emerged. As the loading continued, some big, scattered cracks occurred; then, some portions of the cracks connected with each other, forming the penetrating cracks. A comparison of cracks in SRM models with different rock ratios revealed that when the rock ratio was low (0% and 10%), the SRMs were mainly controlled by soil. Obvious shear zones and large connected cracks were inside the models. When the rock ratio was high (20%, 30% and 50%), because of the rock influence, the cracks mainly had a short length and were concentrated in certain portions near the model edge. In addition, there were no obvious shear zones.

**Fig. 16** PFC3D simulation results of 3D crack growth in SRM▶ (Transparent light gray represents soil particles, and opaque dark gray indicates rock particles; the blue and green disks represent tensile cracks and shear cracks, respectively. The rows from **a–e** represent five different rock ratios of 0%, 10%, 20%, 30% and 50%, respectively. The images from left to right of each row show the crack distribution and growth when the applied load reached the levels of null, peak load, 70% post-peak load, 40% post-peak load and 20% post-peak load; in addition, the rock particles of the null load are marked according to the CT images.)

### 4.3 Rock translation and rotation

The simulation results revealed that rock gravels inside the SRM had translated and rotated during the loading process. To clearly present and analyze the particle movement inside SRM, a partial region of the vertical section of the unloading 50% rock ratio SRM was enlarged, and different colors were used to represent different rocks in that region, as shown in Fig. 19. Figure 20 demonstrates the rock movement within the region (panel) of concern during the loading process. Panels (a)–(c) reveal that before the peak load was reached, the rock gravels mostly moved downward, indicating that the SRM was compressed and there were few rotations and horizontal translations. From panel

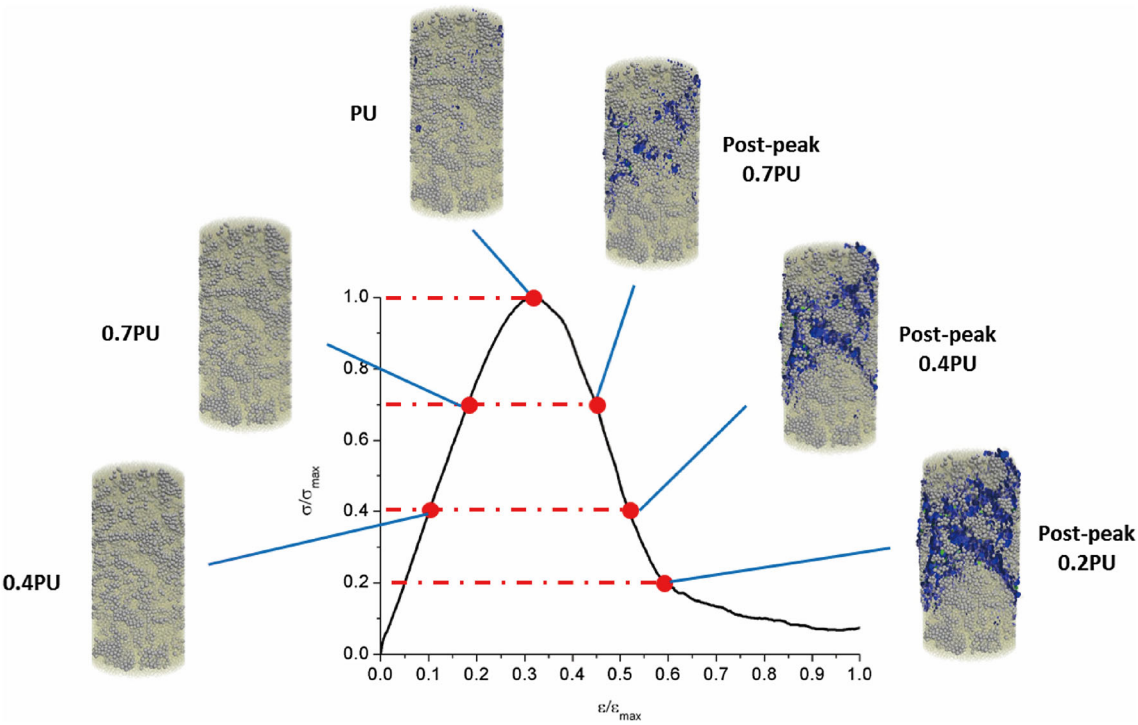


**Fig. 15** Illustration of the loading and simulation stages

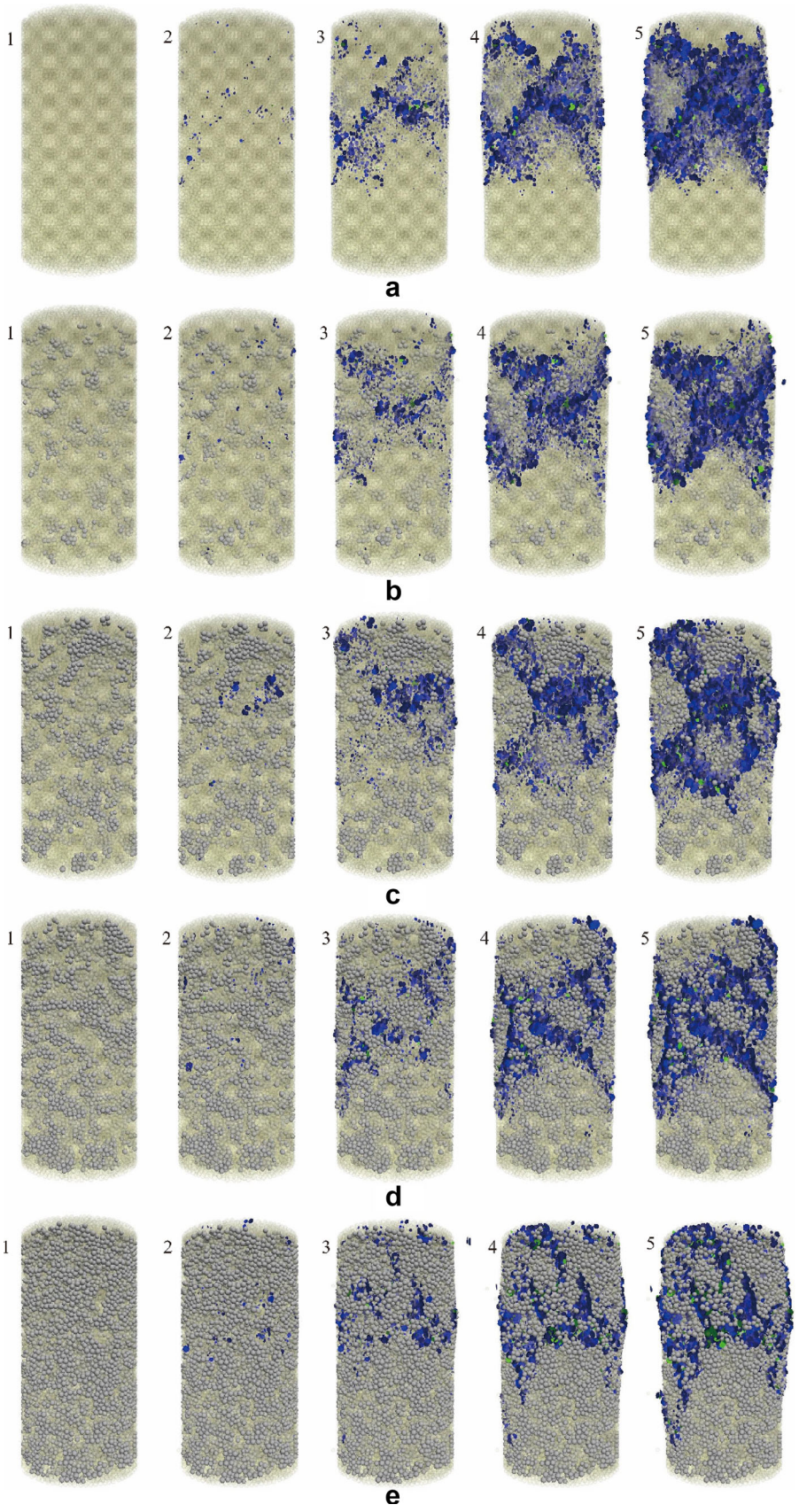
1
2
3
4
5
a
b
c
d
e

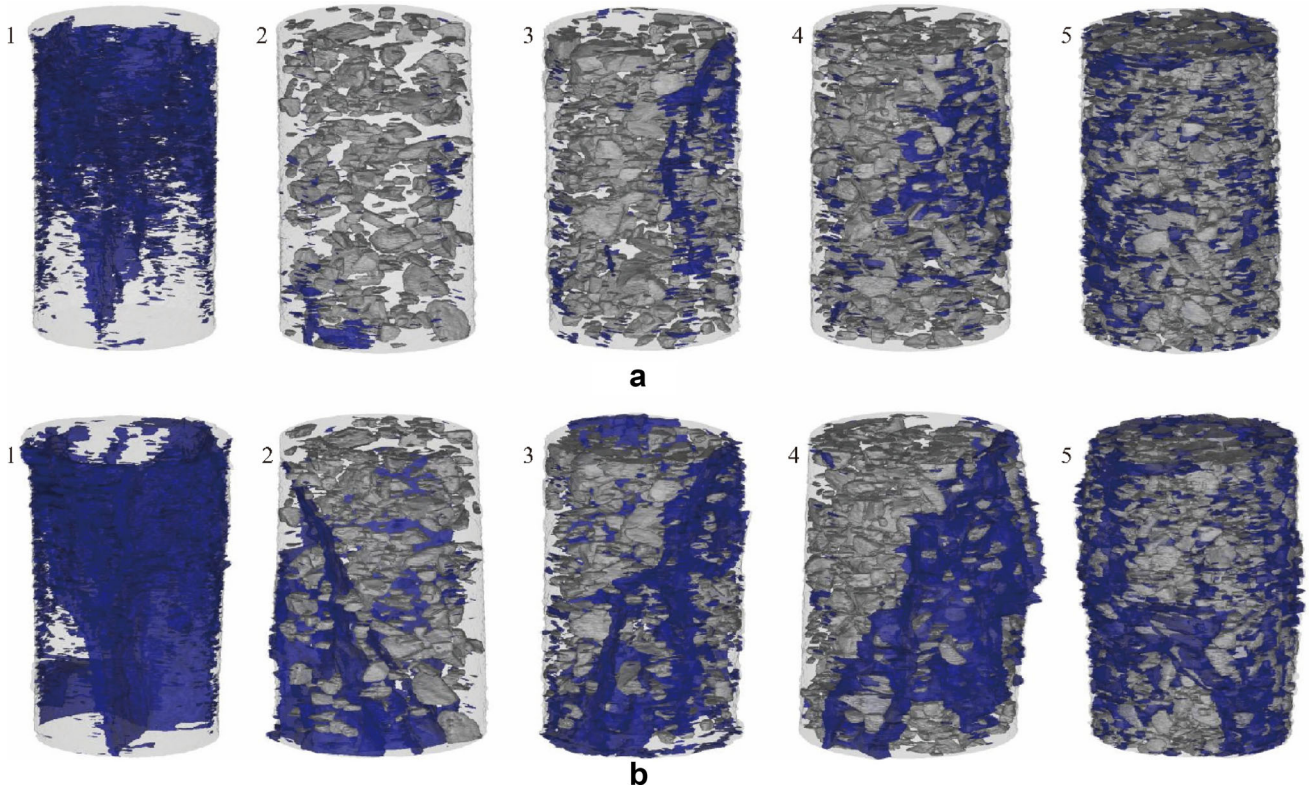


**Fig. 17** CT images of 3D crack distribution and growth in SRM (Blue, dark gray and transparent light gray represent the crack, rock and soil, respectively. Rows **a** and **b** show the crack distribution and growth when the applied load reached the levels of peak load and 40% post-peak load)

(d) to panel (f), when the peak load was reached, the rock gravels exhibited obvious horizontal translation, as well as some rotation, which indicated the lateral expansion of SRM. Taking the green rock gravel as an example, during the loading process, its position became closer to the bottom and right side of the image, which meant that the green rock gravel was translated vertically and horizontally. From panel (d) to panel (f), a green particle became progressively larger, which indicated that the green rock gravel was rotated or translated perpendicularly to the image. Obvious rock rotation of the pink and red rock gravels can be observed in panels (e) and (f).

### 4.4 Strength and elastic modulus

Table 3 compares the results of strength and elastic modulus of the numerical simulation with those of the CT tests. It is shown that, unfortunately, a difference exists between the numerical simulation results and the CT experiment results. The causes for this inconsistency, from authors' points of view, are possibly due to: (1) the loading processes were not identical. The load was applied piecewise in the CT tests but continuously in the simulation, and (2) the strength of the soil/rock interface may not be consistent with the real value. Setting the parameters of the soil/rock interface to be identical to those of the soil/soil contact bond could have some influence on the results. These problems are expected to be solved in future studies.

## 5 Conclusions

This paper proposed a novel numerical method to construct a three-dimensional SRM model in PFC3D representing the real complex structure of SRM. A μCT technique was used to acquire the real structural information and to identify the entire deformation and failure processes of SRM under uniaxial compressive loads. We developed an image-processing program to improve CT images and to extract the internal structure information of SRM specimens. By conducting the secondary development with FISH programming in the PFC3D platform, the real 3D SRM structure models were built using the attained CT information. Each rock clump in the model has its own unique shape resembling the counterpart rocks in the real SRM specimen. The comparison between the PFC3D model and the prototype shows good consistency. The real heterogeneity and irregular structure of SRM can be represented by the PFC model.

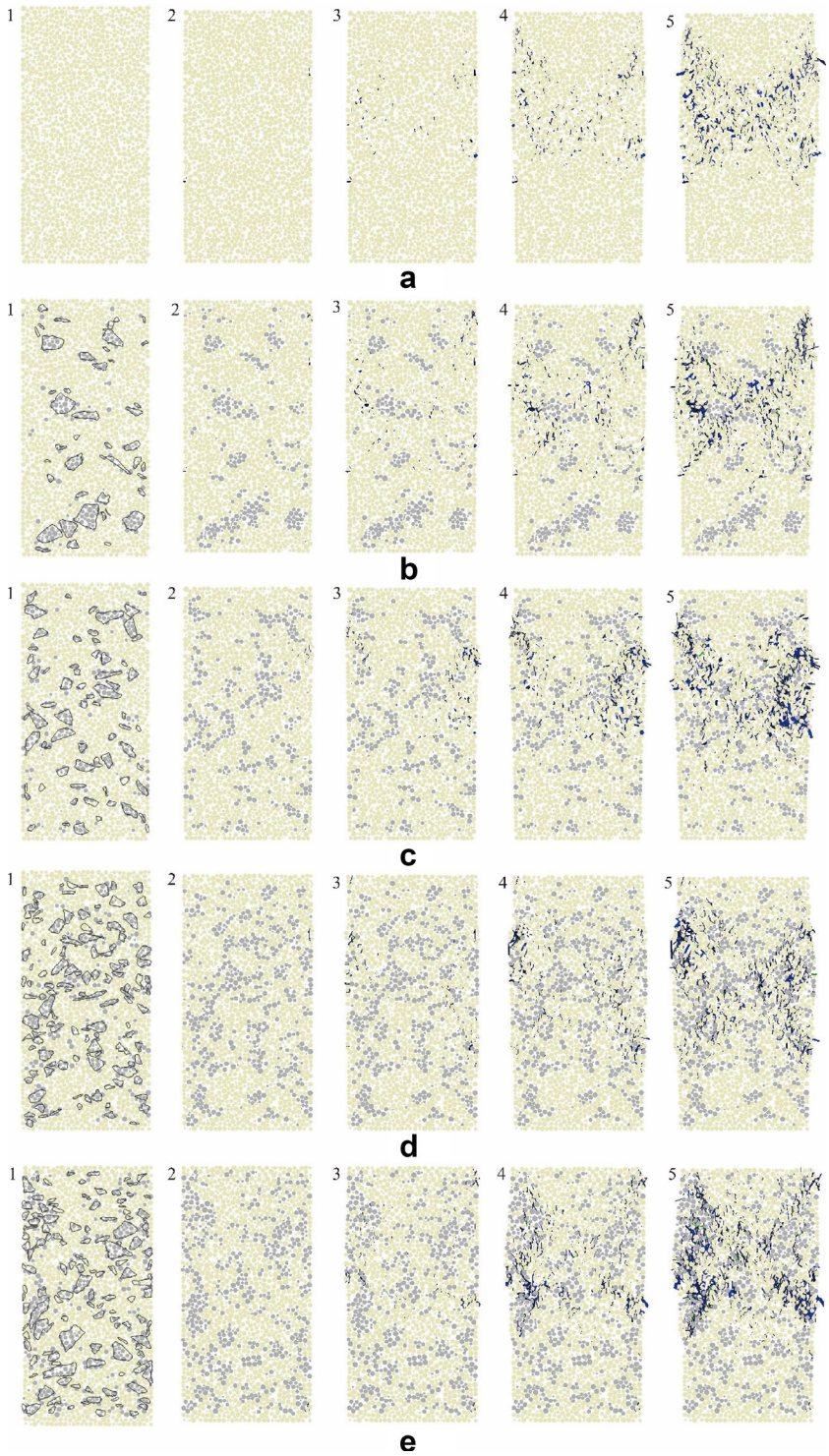


**Fig. 18** Vertical sectional representations of 3D crack distribution and growth in PFC3D models of SRM (Light yellow and gray represent soil particles and rock particles, respectively, while the short lines with the other dark color refer to cracks. Rows **a**–**e** represent five different rock ratios of 0%, 10%, 20%, 30%, and 50%, respectively. The images from left to right of each row show the crack distribution and growth when the applied load reached the levels of null, peak load, 70% post-peak load, 40% post-peak load and 20% post-peak load. The rock geometries at the unload stage are marked according to the CT images)

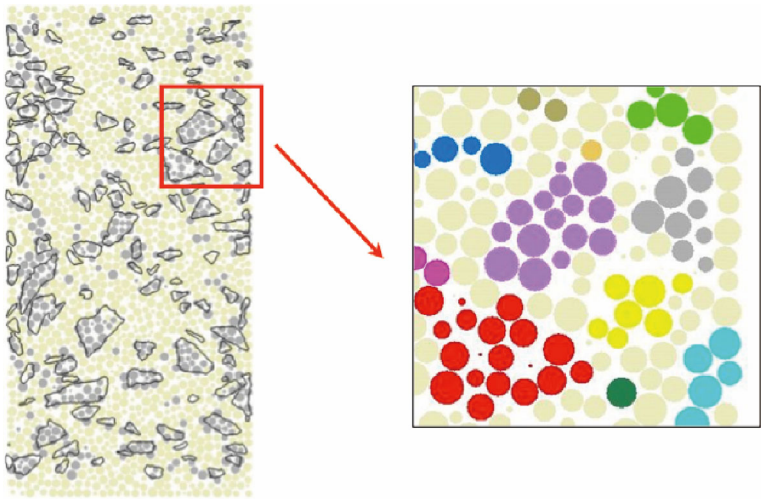

**Fig. 19** Partial enlargement panel showing the positions of rock particles

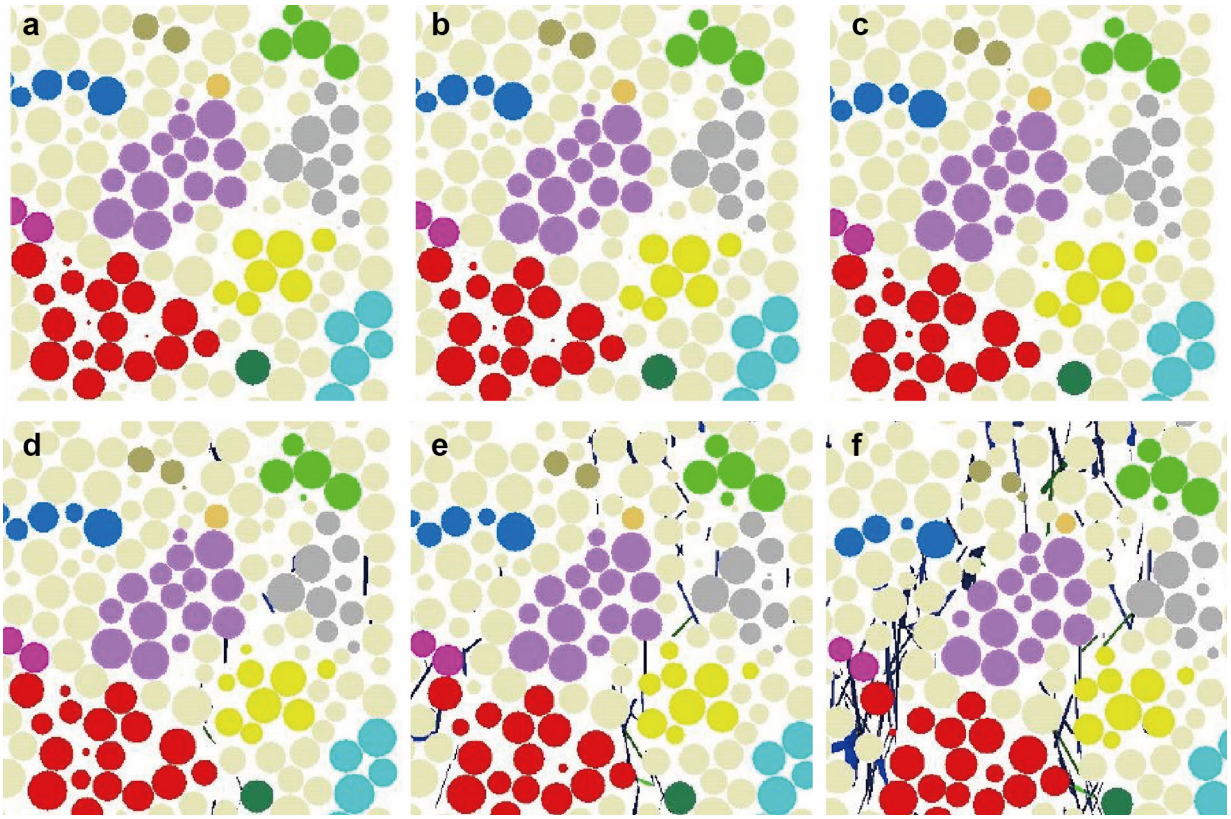


**Fig. 20** Illustration of rock translation and rotation (Panels **a–f** refer to 40% peak load, 70% peak load, peak load, 70% post-peak load, 40% post-peak load, and 20% post-peak load, respectively)

Based on the PFC models, the entire compression-induced failure process was simulated in PFC3D. The results revealed that the SRM failure patterns in the numerical simulation and CT tests have much similarity. Based on the simulation results, it can be concluded that the rock ratio is an important factor that influences the SRM failure patterns

**Table 3** Comparison between the numerical simulation results and the CT experiment results

| Rock ratio (%) | 0 | 10 | 20 | 30 | 50 |
|---|---|---|---|---|---|
| Strength of the CT test (MPa) | 1.09 | 2.80 | 2.22 | 2.44 | 1.17 |
| Strength of the simulation (MPa) | 1.08 | 1.15 | 1.20 | 1.35 | 1.49 |
| Elastic modulus of the CT test (MPa) | 76.7 | 122.0 | 72.7 | 83.0 | 76.6 |
| Elastic modulus of the simulation (MPa) | 77.9 | 86.7 | 96.1 | 103.0 | 122.2 |

and mechanisms. Furthermore, PFC3D shows great advantages in simulating the translation and rotation of particles or blocks.

**Acknowledgements** The authors gratefully acknowledge the financial support from the State Key Research Development Program of China (Grant No. 2016YFC0600705), the National Natural Science Foundation of China (Grant Nos. 51674251, 51727807, 51374213), the National Natural Science Foundation for Distinguished Young Scholars of China (Grant No. 51125017), the Fund for Creative Research and Development Group Program of Jiangsu Province (Grant No. 2014-27), and the Priority Academic Program Development of Jiangsu Higher Education Institutions (Grant No. PAPD2014), and an open project sponsored by the State Key Laboratory for Geomechanics and Deep Underground Engineering (Grant SKLGDUE K1318) for their financial support.



## References

Bian H, Jia Y, Armand G, Duveau G, Shao J-F (2012) 3D numerical modelling thermo-hydromechanical behaviour of underground storages in clay rock. Tunn Undergr Space Technol 30:93–109

Börgesson L, Johannesson L-E, Gunnarsson D (2003) Influence of soil structure heterogeneities on the behaviour of backfill materials based on mixtures of bentonite and crushed rock. Appl Clay Sci 23:121–131

Casagli N, Ermini L, Rosati G (2003) Determining grain size distribution of the material composing landslide dams in the Northern Apennines: sampling and processing methods. J Eng Geol 69:83–97

Chen Z, Chen S, Chen J, Sheng Q, Yan H, Hu W (2012) In-situ double-ring infiltration test of soil–rock mixture. J Yangtze River Sci Res Inst 29:52–56

Cheng G-W, He J-M, Li X, Di B-R, Li S-D (2010) Particle flow simulation for soil–rock mixtures under biaxial pressure. Min Metall Eng 30:1–4

Cho NA, Martin C, Sego D (2007) A clumped particle model for rock. Int J Rock Mec Min Sci 44:997–1010

Coker DA, Torquato S, Dunsmuir JH (1996) Morphology and physical properties of Fontainebleau sandstone via a tomographic analysis. J Geophys Res Solid Earth 101:17497–17506

Ding X, Li Y, Wang X (2010) Particle flow modeling mechanical properties of soil and rock mixtures based on digital image. Chin J Rock Mech Eng 29:477–484

Ding X, Zhang H, Huang S, Lu B, Zhang Q (2012) Research on mechanical characteristics of unsaturated soil–rock mixture based on numerical experiments of mesostructure. Chin J Rock Mech Eng 31:1553–1566

Erguler Z, Ulusay R (2009) Water-induced variations in mechanical properties of clay–bearing rocks. Int J Rock Mech Min Sci 46:355–370

Fakhimi A (2009) A hybrid discrete–finite element model for numerical simulation of geomaterials. Comput Geotech 36:386–395

Fu W, Cai J-J, Dong H, Wang A-H, Liu H-Q, Wang L-Y, Tian H (2004) Current status of numerical simulation of granular flow. J Mater Metall 3:172–175

Gan Y, Kamlah M (2010) Discrete element modelling of pebble beds: with application to uniaxial compression tests of ceramic breeder pebble beds. J Mech Phys Solids 58:129–144

Ghorbani A, Zamora M, Cosenza P (2009) Effects of desiccation on the elastic wave velocities of clay–rocks. Int J Rock Mech Min Sci 46:1267–1272

Guo J, Xu G, Jing H, Kuang T (2013) Fast determination of meso-level mechanical parameters of PFC models. Int J Min Sci Technol 23:157–162

Hadjigeorgiou J, Esmaieli K, Grenon M (2009) Stability analysis of vertical excavations in hard rock by integrating a fracture system into a PFC model. Tunn Undergr Space Technol 24:296–308

He J (2004) Study of deformation and failure mechanisms of rock–soil aggregate in three gorges reservoir area. Dissertation, China University of Mining and Technology, Beijing

He J-M, Li X, Wu J-B, Cheng G-W, Xu J-F (2009) Modeling method of the rock–soil aggregate and its numerical test. Min Metall Eng 29:1–78

Heim A (1882) Der Bergsturz von Elm. Z Deutsch Geol Gesells 34:74–115

Hu M, Wang R, Chen Z, Wang Z (2010) Initiation process simulation of debris deposit based on particle flow code. Rock Soil Mech 31:394–397

Itasca_Consulting_Group (1999a) PFC3D—theory and background

Itasca_Consulting_Group (1999b) PFC3D—use's guide

Itasca_Consulting_Group (1999c) PFC3D—verification problems and example applications

Kuenza K, Towhata I, Orense RP, Wassan TH (2004) Undrained torsional shear tests on gravelly soils. Landslides 1:185–194

Kulatilake P, Malama B, Wang J (2001) Physical and particle flow modeling of jointed rock block behavior under uniaxial loading. Int J Rock Mech Min Sci 38:641–657

Lanaro F, Tolppanen P (2002) 3D characterization of coarse aggregates. Eng Geol 65:17–30

Li X, Liao Q, He J (2004) In-situ tests and a stochastic structural model of rock and soil aggregate in the three gorges reservoir area, China. Int J Rock Mec Min Sci 41:702–707

Li X, Liao Q-L, He J-M, Chen J (2007) Study on in situ tests of mechanical characteristics on soil–rock aggregate. Chin J Rock Mech Eng 26:2377–2384

Liao Q, Li X, Hao Z, Wang S, Wu M, He J (2006) Current status and future trends of studies on rock and soil aggregates (RSA). J Eng Geol 14:800–807

Lin P-S, Chang C-W, Chang W-J (2004) Characterization of liquefaction resistance in gravelly soil: large hammer penetration test and shear wave velocity approach. Soil Dyn Earthq Eng 24:675–687

Liu Y, Liu Q, Chen H, Gong X, Zhang D, Yao D, Li L (2005) Numerical study on rainfall infiltration in rock–soil slop. Sci China Ser E: Technol Sci 48:33–46

Liu Z, Zhou N, Zhang J (2013) Random gravel model and particle flow based numerical biaxial test of solid backfill materials. Int J Min Sci Technol 23:463–467

Lu M, McDowell G (2007) The importance of modelling ballast particle shape in the discrete element method. Granul Matter 9:69–80

Luo Y, Gong X-N, Lian F (2008) Simulation of mechanical behaviors of granular materials by three-dimensional discrete element method based on particle flow code. Chin J Geotech Eng 30:292–297

Ouyang Z-H, Li S-H, Dai Z-S (2010) On the influence factors of mechanical properties for soil–rock mixture. J Exp Mech 25:61–67

Potyondy D, Cundall P (2004) A bonded-particle model for rock. Int J Rock Mech Min Sci 41:1329–1364

Shang Y, Yang Z, Liao Q (2001) Geological hazard distribution and prevention in North of Brahmaputra Canyon, Tibet. Chin J Geol Hazard Control 12:30–40

Shu Z, Liu X, Liu B, Guo Z (2009) Study of strength properties of earth-rock aggregate based on fractals. Chin J Rock Mech Eng 28:2651–2656

Spanne P, Thovert J, Jacquin C, Lindquist W, Jones K, Adler P (1994) Synchrotron computed microtomography of porous media: topology and transports. Phys Rev Lett 73:2001–2004

Sun HF, Yang ZK, Xing MX, Ju Y, Yang YM CT (2012) Investigation of fracture mechanism of soil–rock mixtures. In: Applied mechanics and materials. Trans Tech Publ, pp 67–71

Sun H, Ju Y, Wang X, Xing M, Zhang Q, Yang Y (2014a) Review of the study on deformation, failure and the mesomechanisms of rock–soil mixture. Sci Chin 44:172–181

Sun H-F, Ju Y, Hang M-X, Wang X-F, Yang Y-M (2014b) 3D identification and analysis of fracture and damage in soil–rock mixtures based on CT image processing. J China Coal Soc 39:452–459

Sun S, Xu P, Wu J, Wei J, Fu W, Liu J, Kanungo DP (2014c) Strength parameter identification and application of soil–rock mixture for steep-walled talus slopes in southwestern China. Bull Eng Geol Env 73:123–140

Vallejo LE, Mawby R (2000) Porosity influence on the shear strength of granular material–clay mixtures. Eng Geol 58:125–136

Wang Y, Li X (2014) Research on damage cracking for rock and soil aggregate using calculation meso-mechanics. Chin J Rock Mech Eng 33:020–024

Wang G, Sassa K (2003) Pore-pressure generation and movement of rainfall-induced landslides: effects of grain size and fine-particle content. Eng Geol 69:109–125

Wang Y, Li X, Hao J (2014) Research status and prospect of rock and soil aggregate. J Eng Geol 22:112–123

Xu R, Hu W (2008) Field horizontal push shear test for mechanical property of soil–rock mixtures under cyclic loading. J Eng Geol 16:63–69

Xu W-j Hu, R-l Yue Z-q, R-j Tan (2009) Genesis and stability of the Zhoujiawan landslide, Three Gorges, China. Bull Eng Geol Environ 68:47–54

Xu W, Zhang H (2013) Research status and development trend of soil–rock mixture. Adv Sci Technol Water Resour 33:80–88

Xu W, Hu R, Tan R, Zeng R, Yu H (2006) Study on field test of rock–soil aggregate on right bank of Longpan in Tiger-Leaping Gorge area. Chin J Rock Mech Eng 25:1270–1277

Xu W-J, Hu R-L, Wang Y-P (2007) PFC2D model for mesostructure of inhomogeneous geomaterial based on digital image processing. J Chin Coal Soc 32:358–362

Xu W, Hu R, Yue Z, Zhang R, Wang G (2008a) Research on relationship between rock block proportion and shear strength of soil–rock mixtures based on digital image analysis and large direct shear test. J Rock Mech Geotech Eng 27:996–1007

Xu W-J, Yue Z-Q, Hu R-L (2008b) Study on the mesostructure and mesomechanical characteristics of the soil–rock mixture using digital image processing based finite element method. Int J Rock Mech Min Sci 45:749–762

Xu W-J, Xu Q, Hu R-L (2011) Study on the shear strength of soil–rock mixture by large scale direct shear test. Int J Rock Mech Min Sci 48:1235–1247

Yin Y (1998) Research on geologic hazards of relocation construction at the Three Gorges Reservoir, the Yangtze River. Chin J Geol Hazard Control 7:59–66

You X (2002) Stochastic structural model of the earth–rock aggregate and its application. Chin J Rock Mech Eng 11:1748–1748

You X-H, Tang J-S (2002) Research on horizontal push-shear in situ test of soil and rock–mixture. Chin J Rock Mech Eng 21:1537–1540

You Z, Adhikari S, Dai Q (2008) Three-dimensional discrete element models for asphalt mixtures. J Eng Mech 134:1053–1063

Yu H, Shen S (2012) Impact of aggregate packing on dynamic modulus of hot mix asphalt mixtures using three-dimensional discrete element method. Constr Build Mater 26:302–309

Yu H, Shen S (2013) A micromechanical based three-dimensional DEM approach to characterize the complex modulus of asphalt mixtures. Constr Build Mater 38:1089–1096

Yue Z, Chen S, Tham L (2003) Finite element modeling of geomaterials using digital image processing. Comput Geotech 30:375–397

Zhao L, Luo H, Li L (2006) Research on application of impact compaction technology to high embankment of highway. Chin J Rock Mech Eng 25:4191–4197

Zhong L (1994) Enlightenments from the accident of Vaiont landslide in Italy. Chin J Geol Hazard Control 5:77–84

Zhou J, Chi Y, Chi Y, Xu J-P (2000) The method of particle flow and PFC2D code. Rock Soil Mech 21:271–273

Zhou J, Zhang L-Q, Dai F-C, Min H (2013) Numerical simulation of direct shear tests for rock and soil mixture in a landslide based on bonded-particle model. Chin J Rock Mech Eng 32:650–652